GEOPHYSICS, VOL. 72, NO. 4 (JULY-AUGUST 2007); P. J31–J41, 12 FIGS.
10.1190/1.2742813

Improving crosshole radar velocity tomograms: A new approach to incorporating high-angle traveltime data

James D. Irving[1], Michael D. Knoll[2], and Rosemary J. Knight[3]

ABSTRACT

To obtain the highest-resolution ray-based tomographic images from crosshole ground-penetrating radar (GPR) data, wide angular ray coverage of the region between the two boreholes is required. Unfortunately, at borehole spacings on the order of a few meters, high-angle traveltime data (i.e., traveltime data corresponding to transmitter-receiver angles greater than approximately 50° from the horizontal) are notoriously difficult to incorporate into crosshole GPR inversions. This is because (1) low signal-to-noise ratios make the accurate picking of first-arrival times at high angles extremely difficult, and (2) significant tomographic artifacts commonly appear when high- and low-angle ray data are inverted together. We address and overcome these two issues for a crosshole GPR data example collected at the Boise Hydrogeophysical Research Site (BHRS). To estimate first-arrival times on noisy, high-angle gathers, we develop a robust and automatic picking strategy based on crosscorrelations, where reference waveforms are determined from the data through the stacking of common-ray-angle gathers. To overcome incompatibility issues between high- and low-angle data, we modify the standard tomographic inversion strategy to estimate, in addition to subsurface velocities, parameters that describe a traveltime 'correction curve' as a function of angle. Application of our modified inversion strategy, to both synthetic data and the BHRS data set, shows that it allows the successful incorporation of all available traveltime data to obtain significantly improved subsurface velocity images.

INTRODUCTION

Crosshole ground-penetrating radar (GPR) traveltime tomography is a popular geophysical method for high-resolution imaging of subsurface electromagnetic (EM) wave velocity. With this technique, a short EM pulse is radiated from a transmitter antenna, located in one borehole, and recorded at a receiver antenna, located in an adjacent borehole. The first-break traveltimes of energy for various configurations of the two antennas are then picked and inverted to obtain an image (tomogram) of the distribution of velocity between the boreholes. Because of the strong contrast that exists between the EM-wave velocity of water (0.03 m/ns) and that of dry earth materials (~0.15 m/ns), the velocities obtained with crosshole GPR tomography are highly correlated with water content in the subsurface. Consequently, the technique is very useful for detecting differences in porosity in the saturated zone, and changes in soil water retention (often linked to changes in grain size) in the vadose zone. Of interest in our research is the use of such information in the development of numerical models for groundwater flow and contaminant transport. Resolution of crosshole GPR tomograms is critical for this application.

In environmental applications, crosshole GPR tomography is commonly performed between boreholes that are spaced quite closely together (on the order of a few meters) (e.g., Peterson, 2001; Alumbaugh and Chang, 2002; Tronicke et al., 2002b). At such borehole spacings, the potential exists in theory for excellent tomographic resolution. This is because, even for the relatively shallow (~20 m) borehole depths typical of environmental applications, close borehole spacings allow for wide angular coverage of the inter-borehole region, which is a key requirement for high-resolution imaging with ray-based tomography (e.g., Menke, 1984; Rector and Washbourne, 1994).

In practice, however, two significant problems are encountered when attempting to take advantage of this wide angular coverage.

Manuscript received by the Editor February 1, 2007; published online June 20, 2007.
[1]Formerly Stanford University, Department of Geophysics, Stanford, California; presently University of Lausanne, Institute of Geophysics, Lausanne, Switzerland. E-mail: james.d.irving@gmail.com.
[2]Formerly Boise State University, Department of Geosciences, Boise, Idaho; presently Boise, Idaho. E-mail: miknoll@gmail.com.
[3]Stanford University, Department of Geophysics, Stanford, California. E-mail: rknight@pangea.stanford.edu.

First, the arrival times of energy traveling at high transmitter-receiver angles (commonly, angles greater than ~50° from the horizontal) are often very difficult to pick because of low signal-to-noise ratios (S/N) in the data. This results not only because of an increased amount of attenuation at high angles arising from longer travel paths, but also because of the radiation patterns of the crosshole GPR antennas, which decrease to zero amplitude along the end-fire directions (e.g., Peterson, 2001; Holliger and Bergmann, 2002). Second, even when high-angle traveltimes can be determined reliably at close borehole spacings, difficulties are commonly encountered when attempting to incorporate these data into crosshole GPR inversions. Specifically, the high-angle data often appear to be incompatible with the lower-angle data available, and cause significant numerical artifacts in the resulting tomograms (Peterson, 2001; Alumbaugh and Chang, 2002; Irving and Knight, 2005a). As a result, current practice is to exclude high-angle traveltime data from crosshole GPR inversions (e.g., Alumbaugh and Chang, 2002; Linde et al., 2006). This has the advantage of allowing reasonable subsurface images to be obtained. However, it comes at the cost of reduced horizontal resolution; high-angle data are necessary to constrain the lateral variability of the subsurface velocity field. Depending on the end use of the crosshole GPR images, this reduction in horizontal resolution may be a serious drawback.

In this paper, we present a case study attempting to address (rather than avoid) the above two issues for a crosshole GPR data set collected at the Boise Hydrogeophysical Research Site (BHRS). To overcome the high-angle picking problem, we develop a strategy for determining first-break times from crosshole GPR data using crosscorrelations. With this technique, picking of the example data set is accomplished automatically and reliably, even for traces with very low S/N corresponding to high transmitter/receiver angles. To address the high-angle incompatibility problem at close borehole spacings, we first discuss what we believe to be the cause of this problem for the BHRS data set. Using this information, we then develop a modified inversion strategy that allows all available traveltimes (both high- and low-angle) to be incorporated successfully into the tomographic reconstruction.

FIELD SITE AND DATA DESCRIPTION

The BHRS is a research wellfield located near Boise, Idaho in a shallow, unconfined aquifer (Barrash et al., 1999). The aquifer consists of an approximately 18-m-thick layer of coarse, unconsolidated, braided-stream deposits (gravels and cobbles with sand lenses), and is underlain by clay and basalt. The purpose of developing the BHRS was to create a site for testing geophysical and hydrologic methods, with the goal of using these methods to characterize the distribution of hydrogeological properties in heterogeneous alluvial aquifers. Eighteen wells have been emplaced at the site, all of which were carefully completed to minimize disturbance of the surrounding formation and cased with 4-in PVC well screen (Barrash and Knoll, 1998). For additional information about the BHRS, including the different stratigraphic units that have been identified using well-log, core, and geophysical data, see Barrash and Clemo (2002), Barrash and Reboulet (2004), Tronicke et al. (2004), Clement et al. (2006), Clement and Barrash (2006), and Moret et al. (2006).

The crosshole GPR field data analyzed in this study were collected at the BHRS between wells labeled A1 and B2 during the summer of 1999. These two wells are approximately 3.5 m apart and 20 m deep. The Malå RAMAC/GPR borehole antennas used for the crosshole survey had a specified center frequency of 250 MHz. To conduct the survey, common-receiver gathers were collected. The receiver antenna, located in well B2, was lowered every 0.2 m. For each receiver location, the transmitter antenna (located in well A1) was fired approximately every 0.05 m as it was lowered down the borehole. The resulting crosshole GPR data set contained over 25,000 traces. Because much of this information is redundant and not necessary to obtain the highest-possible-resolution ray-based tomographic image, we considered data from every fourth transmitter location in our analysis. Subsampling in this manner made the depth-sampling intervals in the transmitter and receiver boreholes approximately equal. In addition, we considered only those traces where both the transmitter and receiver antenna elements were contained entirely below the water table (determined using a water level meter to be at approximately 3 m depth at the time of the survey). The final data set analyzed, representative of the saturated zone between 3.6 and 18.2 m depth, contained 5329 traces with transmitter/receiver angles ranging from −75° to +75° from the horizontal.

To account for borehole deviations in our analysis — a critical step in crosshole GPR tomography, especially at close borehole spacings (Peterson, 2001) — borehole trajectories in the subsurface were measured carefully using a magnetic deviation logging tool. To minimize deviations of the transmitter and receiver locations from the tomographic plane, we applied a very slight coordinate rotation to the data such that, in the new coordinate system, all borehole deviations were constrained to within 3 cm of this plane. Parameters for the rotation were determined using an inversion that minimized the sum of the squared out-of-plane deviations. Finally, the GPR system sampling frequency and transmitter fire time were determined carefully before the survey by firing the antennas in air in a walkaway survey using a calibrated survey tape.

CROSSCORRELATION PICKING OF TRAVELTIMES

Figure 1 shows an example common-receiver gather from the BHRS data set, corresponding to a receiver depth of 5.33 m. All traces in the gather have been normalized by their maximum amplitudes for easier comparison. The figure clearly illustrates why difficulties are often encountered when attempting to pick first breaks in high-angle crosshole GPR data. Notice that when the antenna depths are similar (near the top of the plot), the recorded waveforms have a very strong S/N and picking of first breaks is straightforward; on the uppermost trace, the first break occurs just before the small positive peak located at approximately 55 ns. However, as the transmitter depth (and thus the angle between antennas) increases, the S/N decreases to the point where, near the bottom of Figure 1, the first-arriving peak cannot even be seen, let alone picked. Although low-pass filtering may be of some help in attempting to pick such noisy traces, the large amount of filtering required for traces with very low S/N often can affect significantly the apparent onset of signal. Another idea might be to pick the point of maximum amplitude on the noisy traces and then back off a prescribed amount to obtain the first breaks. However, such picking is not robust. More importantly, the position of the first break with respect to the trace maximum will vary with transmitter/receiver angle because the GPR waveform changes with angle. Clearly, signal is present in the lower traces of Figure 1; its onset is simply overshadowed by noise. The question is: Can we find a way to use what signal is there to estimate the first arrivals?

One solution for the robust estimation of traveltimes in the presence of significant noise, that has been used widely in earthquake and exploration seismic studies, is the crosscorrelation technique (e.g., Peraldi and Clement, 1972; VanDecar and Crosson, 1990; Woodward and Masters, 1991; Molyneux and Schmitt, 1999). With this method, the discrete crosscorrelation of a trace and a high-quality reference waveform (having a known arrival time) is determined, and then the difference in traveltime between the two signals is obtained from the time shift at which the crosscorrelation value is a maximum.

Ideally, the reference waveform used with this technique should be noise-free and have the same shape as the waveform present on the trace in question. Although synthetics are often used to obtain such a waveform in earthquake studies, we obtained reference waveforms for crosscorrelation picking of the BHRS data set from the data themselves. We found that synthetic modeling required too much knowledge about GPR system, antenna, and earth parameters to yield waveforms that were sufficiently close enough to those in the field data for effective crosscorrelation analysis. To obtain the reference waveforms, we stack traces that have been aligned on the first arrival. Because the GPR pulse changes with transmitter/receiver angle (a result of variations in antenna radiation and reception with angle, and likely also propagation dispersion along travel paths having different lengths), we determine a number of different reference waveforms that represent ranges in angle where the arriving pulses have similar shape.

Figure 2 is a flowchart illustrating the sequence of steps involved in our crosscorrelation picking procedure. The crosshole GPR data are first preprocessed by removing any DC offset from each trace (determined from the mean value of the trace before the onset of signal) and by normalizing each trace by the signal maximum (estimated by low-pass filtering the data and finding the maximum value). If desired, extremely noisy traces with no apparent signal can be discarded straightaway to reduce the number of bad picks obtained with the technique. Next, the crosshole data are sorted into common-ray-angle gathers (e.g., Pratt and Worthington, 1988; Pratt and Goulty, 1991; Tronicke et al., 2002a). To do this, we create a set of angle bins and place each trace into the appropriate bin based on the transmitter/receiver angle. To determine a high-quality reference waveform for each angle bin, the waveforms in each gather must be aligned and then stacked.

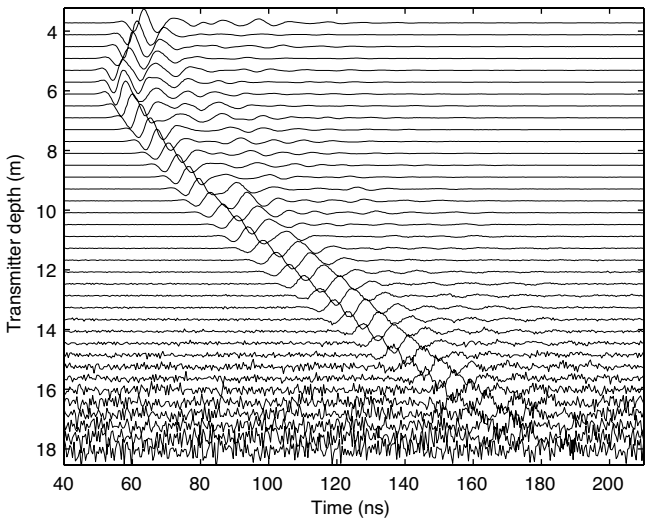

Figure 1. Common-receiver gather from the BHRS data set showing the difficulties in picking first-break times at high transmitter-receiver angles arising from low S/N. Receiver depth is 5.33 m. All traces have been normalized by their maximum values.

Because aligning the traces requires some means of estimating the relative time shifts between the waveforms, we use crosscorrelations, but in an iterative manner as follows: Initially, the traces in a common-ray-angle gather are aligned by crosscorrelating them with the trace in the gather having the highest S/N. This places the majority of traces into proper alignment, which allows for a higher quality waveform to be obtained through stacking. In the second iteration, traces in the gather are aligned again, but this time by crosscorrelating them with the mean trace from the previous iteration. This process can be continued until the vast majority of traces in a gather are properly aligned; however, we have found that two iterations are usually sufficient.

Once the reference waveforms for each angle range have been determined, their first arrivals are picked manually. The entire crosshole data set is then picked automatically by crosscorrelating each trace with the appropriate reference waveform. To increase the robustness of this algorithm, we limit the number of lags used in the crosscorrelations to reasonable values (i.e., for the BHRS data set, absolute differences in arrival time between individual traces and the reference trace were assumed to be less than 20 ns). As a final step, all of the automatic picks made with this method should be checked visually for accuracy. Bad picks are generally quite obvious, as they

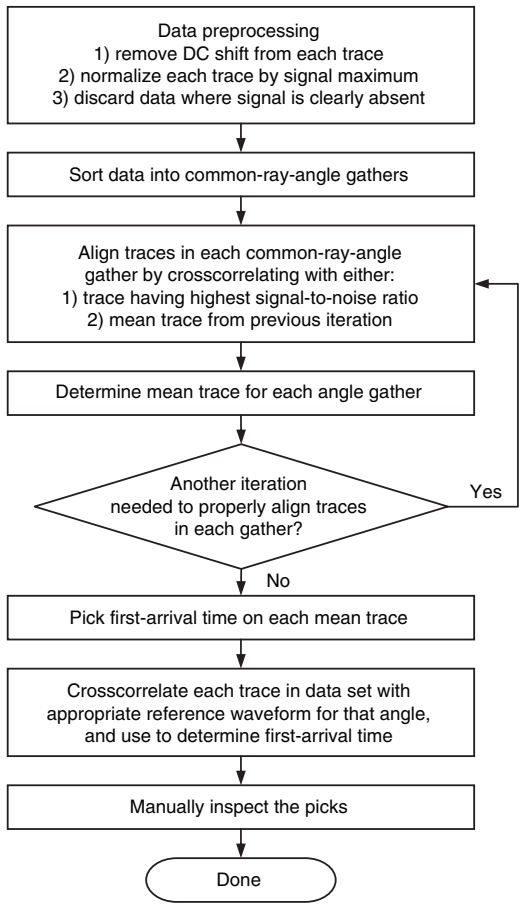

Figure 2. Flowchart of our crosscorrelation picking procedure.

tend to be caused by the crosscorrelation being maximized when the two signals are mismatched by a full cycle.

As an example, Figure 3a shows one of the common-ray-angle gathers obtained from the BHRS data set for the 65° to 70° angle range. Here, the transmitter/receiver angle is measured from the horizontal with positive angles representing the case where the receiver antenna is located above the transmitter antenna. Two iterations of crosscorrelating were used to align the traces in this high-angle gather. The waveforms in the gather are clearly visible and have very similar shapes, but they are contaminated by significant amounts of noise which makes picking the first breaks extremely difficult. Figure 3b, on the other hand, shows the mean trace that was obtained by stacking the 322 traces in Figure 3a together. Here, we see that the S/N has been greatly increased and that a small, positive, first-arrival peak, not clearly visible on any individual trace, is now easily identified. The much higher S/N of this mean trace, and the fact that its first break can be picked easily, make it an excellent reference waveform for crosscorrelation analysis.

Figure 4 shows the mean traces that were obtained in the above manner for each angle group in the BHRS data set. The waveforms have been aligned on their manually picked first arrivals for easier comparison. Angle bins were created for every 5° increment from −75° to +75°, which yielded 30 reference waveforms. Figure 4 clearly shows why we must determine these waveforms as a function of angle when picking crosshole GPR data, as opposed to using a single reference waveform for the entire data set; there is a significant change in shape of the GPR pulse with angle that must be accounted for. Also notice that all of the reference waveforms in Figure 4, including the ones on both ends if scaled enough in amplitude, have first-arrival times that are easily identified.

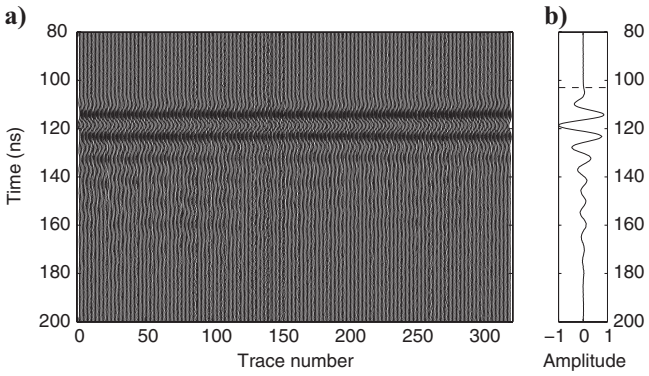

Figure 3. (a) Common-ray-angle gather and (b) mean trace for the 65° to 70° angle range in the BHRS data set. The picked first-arrival time on the mean trace is indicated with a horizontal dashed line.

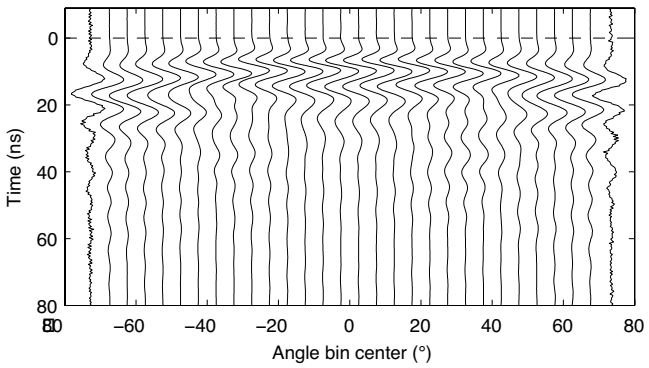

Figure 4. Mean traces determined for the BHRS data set by stacking the different common-ray-angle gathers. The traces have been aligned at $t = 0$ on their picked first arrivals and normalized by their maximum values.

Finally, Figure 5 shows four example receiver gathers from the BHRS data set upon which the first-break times, all determined automatically with our technique, have been superimposed in red. In all of the gathers, the picks are seen to be very reasonable. This is despite the fact that significant noise is present at high transmitter/receiver angles, and in many cases, the positive first-arrival peak at these angles cannot be visually identified. We conclude that picking of the BHRS data using crosscorrelations was a very effective means of determining first-arrival times.

In using crosscorrelations to pick first breaks as described above, we implicitly assume that waveforms recorded at similar transmitter/receiver angles have similar shapes, and are thus suitable for stacking to obtain useful, high-quality reference waveforms. This assumption is valid only in the absence of very sharp velocity contrasts in the subsurface, as such velocity contrasts can give rise to strongly scattered arrivals that interfere with the direct-arriving pulse. Indeed, the BHRS data shown in Figures 3–5 were collected entirely below the water table and were void of any strongly scattered arrivals, as evidenced by the similarity of direct-arriving pulses in each angle gather and the success of the crosscorrelation picking. Had the survey region spanned the water table (a very large velocity contrast) or had the antenna positions been nearer to the very reflective air/earth boundary, problems could have been encountered with the picking of some traces. It may be possible to overcome such problems (and thus extend the technique to data sets with significant scattering) through a modification of the algorithm, or by filtering the data beforehand to remove the scattered arrivals. This is a topic of future research.

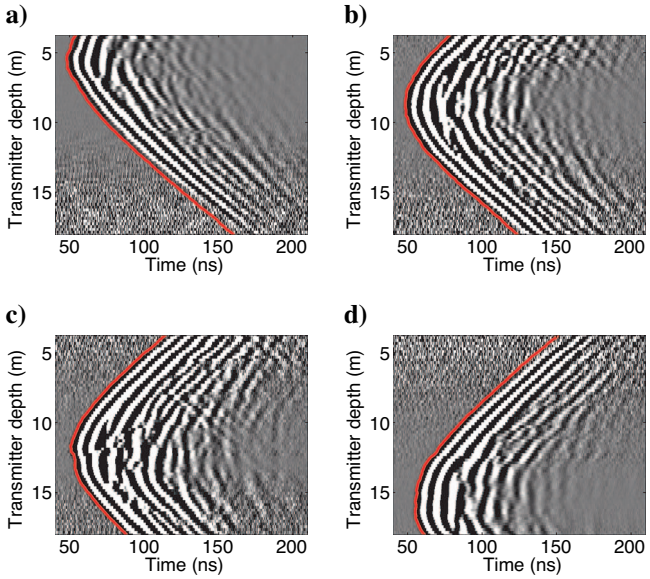

Figure 5. Four common-receiver gathers from the BHRS data set showing the results of our crosscorrelation picking procedure. Picked first breaks are shown in red; (a) receiver depth = 5.33 m; (b) receiver depth = 8.73 m; (c) receiver depth = 12.33 m; (d) receiver depth = 15.53 m.

INCOMPATIBILITY OF HIGH-ANGLE DATA

Next we address the second problem encountered when attempting to take advantage of the wide angular coverage provided by close borehole spacings: the fact that high-angle traveltime data often appear to be incompatible with lower-angle data. Significant insight can be gained into this problem through velocity-versus-angle plots, where the average velocity calculated along each ray in a crosshole GPR data set (assuming a straight path between the antenna centers) is plotted as a function of the transmitter/receiver angle. Figure 6 shows such a scatter plot for the BHRS data set. The figure was created using the picks obtained with the crosscorrelation technique just described. Notice the general trend that exists in velocity with angle for these data; the along-the-ray velocities at high transmitter/receiver angles are markedly greater than those determined for lower angles. This trend clearly illustrates why problems are encountered when high- and low-angle traveltimes are inverted together; the two types of data are providing inconsistent information about the subsurface velocity field. Reasonable subsurface velocity models (that do not possess significant amounts of anisotropy) should not give rise to large-scale trends in velocity with angle.

We have found that the trend seen in Figure 6 is typical of crosshole GPR data collected between closely spaced boreholes (see also Peterson, 2001). Although Peterson (2001) suspects that such a trend is caused by refracted waves that travel partly through air-filled boreholes and arrive before the direct pulse, the BHRS data shown here were collected between water-filled wells where this should not be a problem. It is also very difficult to explain the trend in Figure 6 by the other factors discussed in Peterson (2001) that can cause apparent variations in velocity with angle in crosshole GPR data. For example, although errors in the calculation of the transmitter fire time and inaccurate borehole location measurements could result in a plot resembling Figure 6, every step was taken to ensure that these measurements were accurate for the BHRS data set. Also, such errors do not explain the consistency we have observed in the trend in Figure 6 across different data sets. In addition, although the presence of anisotropy can give rise to general trends in velocity with angle, geologically reasonable anisotropy (i.e., due to thin horizontal layering) results in velocities that are greater at low angles, which is the opposite of what we observe. Finally, it is unlikely that the trend in Figure 6 is the simple result of having less-accurate traveltime picks at high transmitter/receiver angles because of decreased S/N. In that case, one would not expect picks to be consistently earlier than the true first-arrival times (which is required to yield higher velocities at high angles). The question, then, is why do we have this trend in velocity with angle for the BHRS data set?

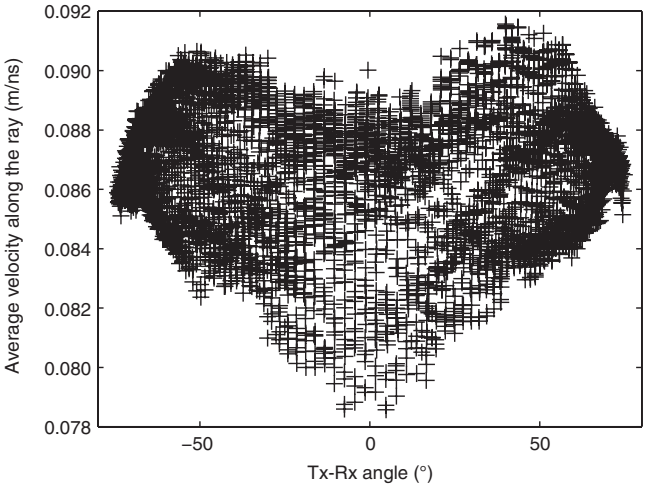

Figure 6. Velocity-versus-angle plot for the BHRS data set.

Recently, Irving and Knight (2005a) addressed the high-angle incompatibility issue in crosshole GPR tomography, and suggested that the problem may result from a common assumption made during the inversion of the data: that first-arriving energy always travels directly between the antenna centers. They proposed that, at high transmitter/receiver angles, first-arriving energy may actually travel via the antenna tips. This will be possible when the velocity of energy traveling along the antennas v_{ant} is greater than the velocity of the subsurface medium between the boreholes v_{med}. Using numerical modeling and considering a number of different borehole diameters and external medium properties, Irving and Knight (2005a) showed that often v_{ant} will be significantly greater than v_{med}, in both air- and water-filled boreholes, for a common commercial GPR antenna design.

As an example of how this affects calculated velocities as a function of angle, Figure 7 shows synthetic waveform gathers and the corresponding velocity-versus-angle curves obtained from those gathers, when it is assumed that first-arriving energy always travels directly between the antenna centers. To generate the gathers in Figure 7, we used the antenna modeling approach of Irving and Knight (2006). The antennas considered are 0.8-m-long, center-fed dipoles that are separated by a horizontal distance of 4 m. The homogeneous medium velocity is 0.06 m/ns, and the velocity along the antennas is 0.11 m/ns. These two velocities are typical of a saturated zone scenario. Constant resistive loading was simulated also along the antennas in the numerical modeling to reduce the width of emitted pulses and better represent commercial GPR antennas.

In Figure 7a and b, we see the waveform gather and velocity-versus-angle curve for the case of a very short (unrealistic) Gaussian an-

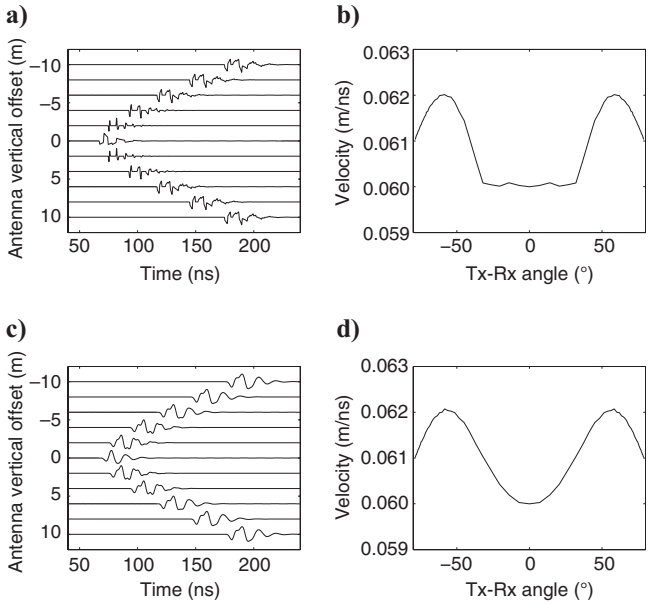

Figure 7. Example waveform gathers and velocity-versus-angle plots (determined from those gathers) for the case of short (a and b) and long (c and d) transmitter feed pulses. Borehole seperation = 4 m, antenna length = 0.8 m, v_{med} = 0.06 m/ns, and v_{ant} = 0.11 m/ns.

tenna feed pulse having a −20 dB width of approximately 1 ns. A number of distinct pulses are visible in the received waveforms, representing radiation and reception at the antenna feed and end points. In the corresponding velocity-versus-angle curve, we see that at low angles, when the assumption about the travel path of first-arriving energy is valid, there is no error in the calculation of the medium velocity (i.e., the velocity curve is flat and equal to the correct value of 0.06 m/ns). However, above some threshold angle when first arrivals actually represent tip-to-tip antenna coupling, errors result because this assumption is invalid. These errors reach some peak value with angle and then begin to decrease in magnitude as the length of the travel path increases. Curves similar in appearance to that in Figure 7b were generated by Irving and Knight (2005a). However, we now believe that such curves do not completely describe crosshole GPR behavior, as they result only when the excitation pulse feeding the transmitter antenna is short in comparison to the length of time required to travel along the antenna arms; this is not likely a realistic scenario in all cases (e.g., Sato and Thierbach, 1991; Ellefsen and Wright, 2005; Liu and Sato, 2005).

In Figure 7c and d, we see the waveform gather and corresponding velocity-versus-angle curve for the case of a longer (more realistic) Gaussian feed pulse having a −20 dB width of approximately 10 ns. In this case, the individual pulses from Figure 7a have merged together. As a result of this interference, the behavior in the corresponding velocity-versus-angle plot (Figure 7d) changes; there is now variation in the calculated velocity across the entire angle range because the effective arrival time of the first pulse is altered by the presence of subsequent pulses (i.e., later-arriving pulses effectively delay the pickable arrival time of the initial pulse). The behavior illustrated in Figure 7d is clearly very similar to the general trend shown for the BHRS data set (minus the scatter), and is what we believe to be the cause of the trend in velocity with angle for these data.

IMPROVED INVERSION PROCEDURE

We saw in the previous section that the incompatibility problem with high-angle data at close borehole spacings results from a general trend in calculated velocity versus transmitter/receiver angle. We believe this trend to result from the flawed assumption that first-arriving energy always travels directly between antenna centers. The challenge now is to develop a tomographic inversion strategy that allows us to use all of the traveltime data available in a crosshole GPR experiment, in order to improve horizontal resolution over the case where high-angle traveltimes are simply discarded. Initially, our approach to this problem involved attempting, through numerical modeling, to estimate accurately the errors associated with tip-to-tip antenna coupling and pulse interference in a crosshole GPR experiment, such that traveltimes and ray geometries could be adjusted accordingly before inverting. Although we found this approach to work very well with synthetic data (Irving and Knight, 2005b), we have since determined that it requires too much knowledge about specific GPR system and antenna details, along with borehole and external medium properties, to be a useful approach for field data. Indeed, all of our attempts to estimate these sources of error accurately for the BHRS data in Figure 6 met with little success. As a result, we chose a simpler approach to invert all available data in crosshole GPR tomography. Because we believe that the high-angle incompatibility problem results from an apparent (incorrect) trend in velocity with transmitter/receiver angle, we set up the tomographic inversion to estimate, in addition to subsurface velocities, parameters that describe a traveltime 'correction curve' as a function of angle. In other words, we allow the inversion to determine a small number of parameters that should largely correct for the angle-related errors in the data.

Standard ray-based traveltime tomography is based upon linking perturbations in traveltime to slowness (inverse of velocity) changes in the subsurface, as shown by the following equation:

$$\Delta \mathbf{t} = \mathbf{L}\Delta \mathbf{s}, \tag{1}$$

where $\Delta\mathbf{t}$ is a vector containing the difference between observed traveltimes and those obtained by ray-tracing through a reference slowness model, $\Delta\mathbf{s}$ is a vector containing the slowness perturbations that must be added to the reference model to fit the observed traveltime data, and $\mathbf{L}$ is the ray-based tomographic sensitivity matrix whose rows contain the length of each ray in every model cell, assuming center-to-center antenna coupling. In our modified inversion procedure, we simply augment equation 1 in the following manner:

$$\Delta \mathbf{t} = [\mathbf{L}\ \mathbf{A}]\begin{bmatrix} \Delta \mathbf{s} \\ \Delta \mathbf{p_a} \end{bmatrix}, \tag{2}$$

where the parameters contained in vector $\Delta\mathbf{p_a}$ are the values of the traveltime correction curve at a set of reference angles, and the rows of matrix $\mathbf{A}$ contain linear interpolation weights to obtain, from these parameters, the traveltime correction for each ray. In using equation 2 for tomography, we implicitly assume that measured traveltimes, once they have been suitably corrected as a function of angle, satisfy equation 1.

To solve equation 2 for the model vector $[\Delta\mathbf{s};\Delta\mathbf{p_a}]$, we form the least-squares normal equations and solve the resulting system using the conjugate-gradient method (e.g., Scales, 1987; Squires et al. 1992). We explicitly impose regularization on the slowness model in this system using second-derivative (smoothness) constraints in the x- and z-directions. If desired, smoothness or symmetry constraints also could be imposed on the traveltime correction curve, although we have generally found such constraints to be unnecessary if the number of parameters describing the curve is kept small. The only constraint on $\Delta\mathbf{p_a}$ that we have found to be absolutely necessary is the enforcement of a zero-traveltime correction for horizontal (zero-angle) rays. Without such a constraint, velocities in the model could be adjusted by some constant value and the offset compensated by an angle-dependent traveltime correction. In forming this constraint, we make the implicit assumption that low-angle traveltimes in the data are accurate. Generally, this should be the case because traveltime data are calibrated in the field using waveforms that are recorded when the antennas are parallel (i.e., at zero angle) and separated in air by some known amount.

As we will see in the next section, the modified inversion strategy described by equation 2 allows us to invert successfully high- and low-angle crosshole GPR data together to obtain tomograms with improved horizontal resolution. This is despite the fact that, in using this strategy, only traveltimes are adjusted as a function of angle and we thus neglect any errors in effective source and receiver positions caused by tip-to-tip antenna coupling. One important limitation to applying angle corrections in this manner is that the technique is not suitable for the inversion of data collected in strongly anisotropic environments. In such environments, large-scale velocity variations as a function of angle are not errors, and an anisotropic inversion code would be necessary to obtain a proper subsurface image. In our expe-

rience, however, strong EM-wave velocity anisotropy in unconsolidated sediments is uncommon. This observation is supported by Peterson (2001).

EXAMPLES

Synthetic data

To demonstrate the effectiveness of our modified inversion strategy, we first apply it to synthetic crosshole GPR data. Figure 8a shows the velocity model we constructed for this example. The model consists of a number of blocks of various sizes having dielectric constants of $\kappa = 22$ (red, 0.064 m/ns) and $\kappa = 28$ (blue, 0.057 m/ns) embedded in a homogeneous background medium having $\kappa = 25$ (green, v = 0.06 m/ns). Electric conductivity throughout the model was set to a constant value of 1 mS/m, and magnetic permeability was assumed to equal its value in free space, μ_0. These electric properties were chosen to represent a saturated zone scenario. Although the model in Figure 8a clearly is not geologically realistic, its blocky structure allows us to examine effectively the differences in resolution attainable using different inversion strategies.

To create the synthetic data, we simulated crosshole GPR transmission and reception through the model in Figure 8a using the finite-difference time-domain (FDTD) technique described in Irving and Knight (2006). The boreholes, located along the left and right sides of the model, were spaced 4 m apart and the transmitter and receiver antennas were located every 0.25 m from 0.5 to 11.5 m depth. Realistic antenna behavior was accounted for in the simulations by replicating, using a superposition of point-electric-dipole source and receiver responses, the antenna current distribution obtained from a finely discretized FDTD simulation. The borehole in the detailed simulation was modeled as a 4-in-diameter, water-filled cylinder. The antenna model considered is a 0.8-m-long, insulated, center-fed dipole, and is described in detail by Irving and Knight (2006). Constant resistive loading was included along the antenna elements such that the waveforms that were produced approximately resembled those we have recorded in field surveys with a similar antenna. The approximate velocity of energy along the model antenna, when located in the water-filled borehole, was 0.11 m/ns. To feed the transmitter antenna, we used a short Gaussian pulse having a -20 dB width of approximately 10 ns.

Once the FDTD simulations were complete, the synthetic cross-hole gathers were automatically picked (a straightforward procedure for noise-free data) and the first breaks were calibrated so that the traveltimes for horizontal ray paths were accurate. At the bottom of Figure 8a, the velocity-versus-angle plot for the resulting data set is depicted. In theory, we should be able to perform very-high-resolution tomographic imaging of the inter-borehole region, because there are traveltime data for angles up to 70° from the horizontal. However, like the plot for the BHRS data in Figure 6, there appears to be a general trend in this figure towards greater velocities at high angles. Again, this trend is the result of assuming that first-arriving energy always travels directly between the antenna centers, when in fact, we have tip-to-tip coupling at high angles and also the effects of interference between feed- and end-radiated pulses.

Figure 8b shows the tomogram and residuals that were obtained when all of the available traveltime data (for high- and low-angle rays) were incorporated into a standard crosshole GPR tomographic inversion (i.e., based on equation 1). For this and each inversion result to follow, regularization parameters were kept constant so that differences in the tomograms would truly reflect differences between the inversion strategies used. Also, because velocity contrasts in the synthetic model are less than 15% and the travel paths are relatively short, straight rays were assumed in the inversions. This assumption has no impact on the generality of our findings, and it significantly simplifies the tomographic imaging. The tomogram in Figure 8b is clearly dominated by numerical artifacts as a result of the incorrect assumption about the travel path of first-arriving energy. In fact, the artifacts are so strong in this case that they completely obscure any reliable subsurface information. The rms error between the tomographic image and true velocity model for this case is 0.0021 m/ns. In the traveltime residuals plot, the imaging problem appears as a W-shaped trend with angle. It is this angular dependence that we address in our modified inversion strategy to allow for the successful incorporation of all available data.

Simply excluding high-angle data from inversions is the usual means of dealing with the high-angle incompatibility problem in crosshole GPR tomography. Figure 8c shows the tomogram and residuals obtained by inverting an aperture-limited ($<30°$) subset of the synthetic data set. Once again, the standard crosshole GPR inversion strategy was employed. Here, a reasonable representation of the input velocity model is clearly obtained, and the rms error between

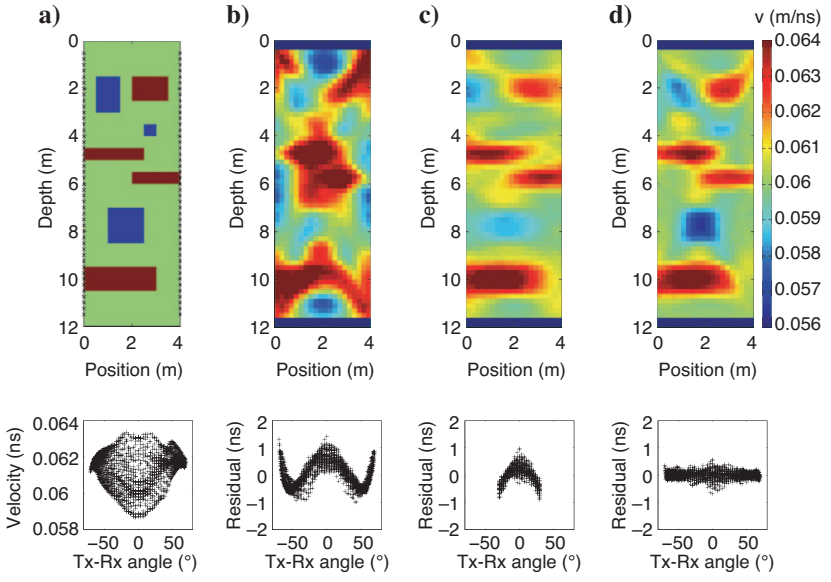

Figure 8. Synthetic data results. (a) Input velocity model and velocity-versus-angle plot for the synthetic data. Transmitter and receiver locations are marked with an x; (b) result of applying the standard crosshole GPR inversion strategy to all available data (rms errror with true velocity model = 0.0021 m/ns); (c) result of applying the same standard inversion strategy to an aperture-limited ($<30°$) subset of the data (rms error = 0.0013 m/ns); (d) result of allowing an angle-dependent traveltime correction in the inversion of all available data (rms error = 0.0010 m/ns). Dark blue areas represent regions with no ray coverage.

the recovered and true models decreases significantly to 0.0013 m/ns. However, because we have not incorporated high-angle rays into the inversion, horizontal resolution is compromised significantly. Most noticeably, the high- and low-velocity anomalies around 2 m depth in Figure 8a are not separated from the edges of the grid in Figure 8c; the small, low-velocity anomaly around 4 m depth cannot be identified; and the large, low-velocity anomaly around 8 m depth is smeared significantly in the horizontal direction. Although more horizontal structure could be added to this tomogram by increasing the cutoff angle for aperture limitation, we found that 30° yielded the best trade-off between an image containing horizontal structure and one with a minimal number of inversion artifacts. Significant angular dependence also is seen in the traveltime residuals in Figure 8c.

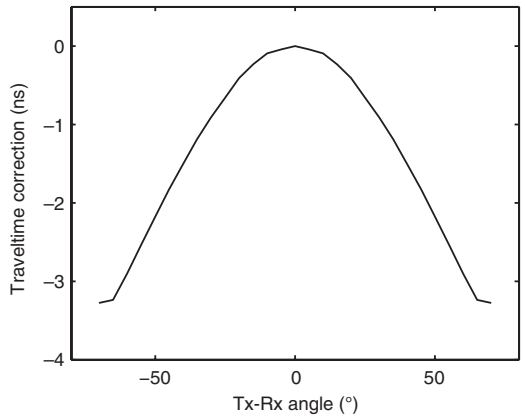

Figure 9. Angle-dependent traveltime correction parameters obtained in the inversion of the synthetic data in Figure 8d.

In Figure 8d, we see the results of applying our modified inversion procedure to all available traveltimes in the synthetic data set. As mentioned, this involves estimating, in addition to subsurface velocities, a set of parameters describing a traveltime correction curve as a function of angle. Notice that, in this case, we obtain a significantly improved result over aperture limitation, and the rms error further decreases to 0.0010 m/ns. All anomalies in the input velocity model can now be seen, and there is far less horizontal smearing present in the tomogram. In addition, the amplitudes of the anomalies in Figure 8d are closer to the true block velocities in Figure 8a.

Clearly, by allowing for an angle-dependent traveltime correction in the inversion, we are able to use effectively the high-angle data to improve tomographic resolution. Further, because of the parameterization with angle, there is no longer an angular trend seen in the traveltime residuals in Figure 8d, and the absolute magnitude of these residuals is significantly less than in Figure 8b. This is not surprising but it does show that, after the traveltime correction, our synthetic data are much better fit by the model described by equation 1. Finally, Figure 9 shows the angle correction parameters obtained with our modified inversion strategy. In this example, we inverted for 30 parameters that were evenly spaced over the angle range of the data, from −70° to 70°. Although no regularization (aside from enforcing a zero-traveltime correction at zero angle) was imposed on these parameters, we see that the traveltime correction curve is smooth and reasonable.

BHRS data set

We now demonstrate the application of our modified tomographic inversion strategy to the BHRS field data set. As with the synthetic example, straight rays were used in all of the following inversion results because velocity contrasts in the subsurface were believed to be less than 20% (typical of the saturated zone), and because the A1 and B2 boreholes at the BHRS are spaced relatively closely together. Regularization parameters were kept constant between inversions so that the relative effectiveness of the different inversion strategies could be evaluated.

Figure 10a shows the tomogram and traveltime residuals obtained when all of the available BHRS data (for ray angles up to 75° from the horizontal) were inverted using the standard crosshole GPR inversion approach. Although numerical artifacts in this image clearly are not as severe as those in our synthetic example in Figure 8b (possibly a result of the fact that shorter, higher-frequency antennas were used for this survey), we see a number of features in Figure 10a that are geologically unreasonable and indicate problems with the inversion. Specifically, in a number of places in the image, there are horizontal discontinuities where it is expected that continuity should exist. Most notable of these are the high-velocity layer between 16 and 18 m, which fades out in the center of the tomogram, and the thick, high-velocity zone between 7 and 12 m, which contains a

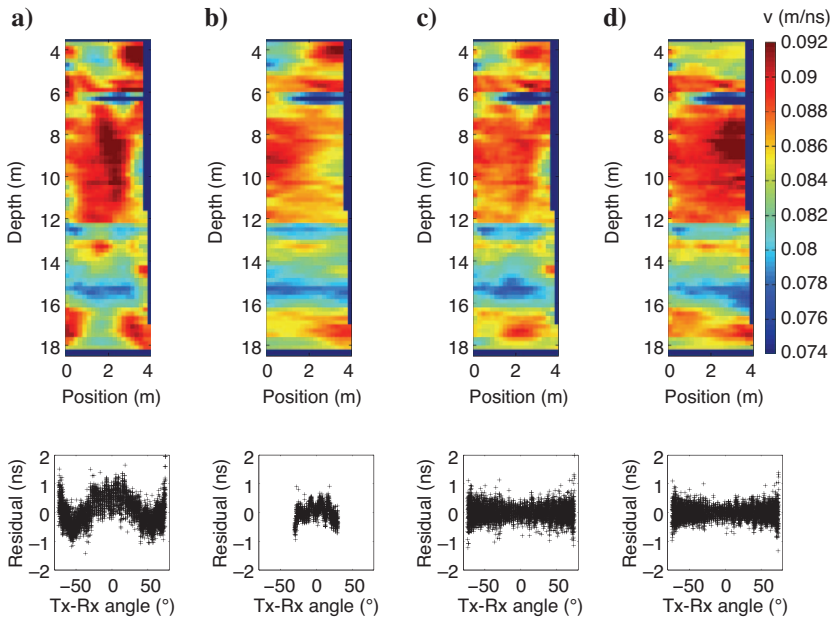

Figure 10. Application to the BHRS data set (well A1 on left, well B2 on right). (a) Result of applying the standard crosshole GPR inversion strategy to all available data; (b) result of applying the same standard inversion strategy to an aperture-limited (<30°) subset of the data; (c) result of allowing an angle-dependent traveltime correction in the inversion of all available data; (d) result of allowing both angle- and receiver-position-dependent traveltime corrections in the inversion of all available data. Dark blue areas represent regions with no ray coverage.

central zone of significantly higher velocity. As with the synthetic example, such problems are manifest in the traveltime residuals plot as a distinct, W-shaped trend with angle. Such a trend should not exist for a proper tomographic inversion.

In Figure 10b, we see the result of applying aperture-limitation to the BHRS data set before inverting. Again, a cutoff angle of 30° was used to obtain the best trade-off between horizontal resolution and a minimal number of obvious inversion artifacts in the image. In this case, we see that the tomogram has become much more geologically reasonable. Layers are now more horizontally continuous and the image lacks the obvious problems seen in Figure 10a. However, because we discarded the high-angle-ray data to produce the inversion result in Figure 10b, we are left wondering whether such horizontal continuity is real, or simply a product of the aperture limitation.

Figure 10c shows the tomogram and residuals obtained when all of the available BHRS traveltimes were incorporated into our modified inversion procedure. Notice that, through the use of an angle-dependent traveltime correction, we are now able to obtain a very reasonable subsurface image that is quite similar in appearance to the aperture-limited result in Figure 10b. For this example, it appears as if the addition of the high-angle data does not provide a large amount of additional structure to the tomogram (i.e., the geology between the boreholes is such that it can be largely captured by the low-angle-ray data). However, because we have used all available traveltimes to create the image in Figure 10c, we have greater confidence that the features seen here are representative of the true subsurface velocity model. As with the synthetic example, the traveltime residuals obtained using our modified inversion procedure are now approximately flat with angle.

Although we consider Figure 10c to be a much improved subsurface image over Figure 10a, there is still something in this tomogram that causes us concern given other geophysical and geologic data collected at the BHRS. This is the fact that the thick, high-velocity zone between 7 and 12 m depth, which is known to be a laterally continuous, poorly sorted sediment layer with relatively little internal variation in porosity (Barrash and Reboulet 2004), shows significant lateral variability in Figure 10c. As a result of this observation, we investigated the effects of further parametrizing the inverse problem to account for possible static traveltime shifts at the receiver locations.

When collecting each gather in the BHRS data set, the receiver antenna was held fixed while the transmitter antenna was lowered down its borehole. Because of this, the potential exists for many traveltimes to be affected by a single error in the location of the receiver antenna in its well, or by differences in the coupling of this antenna with its surroundings. For example, a horizontal movement of the receiver antenna in its well by only 2.5 cm (when the well is filled with water) will result in a shift in measured traveltime of at least 0.75 ns for all of the traces in that receiver gather. This shift is quite significant when the borehole spacing of only 3.5 m is considered. In addition, slight drifts in the transmitter fire time over the duration of the crosshole survey can result in static time shifts between different receiver gathers.

To estimate traveltime corrections at each receiver location in addition to slownesses and angle-correction parameters, we further augmented equation 2 as follows:

$$\Delta \mathbf{t} = [\mathbf{L}\ \mathbf{A}\ \mathbf{R}] \begin{bmatrix} \Delta \mathbf{s} \\ \Delta \mathbf{p_a} \\ \Delta \mathbf{p_r} \end{bmatrix} \tag{3}$$

where the vector $\Delta \mathbf{p_r}$ contains receiver position traveltime corrections (i.e., a static correction for each receiver position), and matrix $\mathbf{R}$ selects, for each ray, which correction to use. Inverting for statics in this manner was shown by Vasco et al. (1997) to be a valuable tool in crosshole GPR tomography. Because there is no reason why such static traveltime shifts should be smooth in depth, we added no smoothness regularization to the inversion. We did, however, enforce smallness in the static correction parameters because a large constant traveltime shift for all receiver locations again could be compensated by appropriate angle-dependent traveltime corrections.

Figure 10d shows the tomogram and residuals for the full BHRS data set, after both angle- and receiver-position-dependent traveltime corrections were estimated in addition to subsurface velocities. We now see that the thick, high-velocity zone between 7 and 12 m depth is more uniform and horizontally continuous, and thus in better agreement with other site data. In addition, the thin, high-velocity layer at approximately 13 m depth is more pronounced than in Figure 10c, and a dipping interface between the low- and high-velocity layers near the bottom of the section can be seen more clearly. We believe the results in Figure 10d to be more reasonable than those shown in Figure 10c, and we will see shortly that they are in better agreement with neutron-porosity log data collected in boreholes A1 and B2. Figure 11 shows the angle- and receiver-position-dependent traveltime corrections that were estimated by the inversion procedure. In the plot of the receiver static corrections versus depth (Figure 11b), we see a general trend of increasingly negative corrections at depths away from ~9 m. This trend may result from a slight drift in the transmitter fire time over the period of the crosshole survey, small inaccuracies in the borehole deviation measurements, or perhaps systematic errors in the location of the receiver antenna caused by cable stretching and compression over the period of the tomography survey.

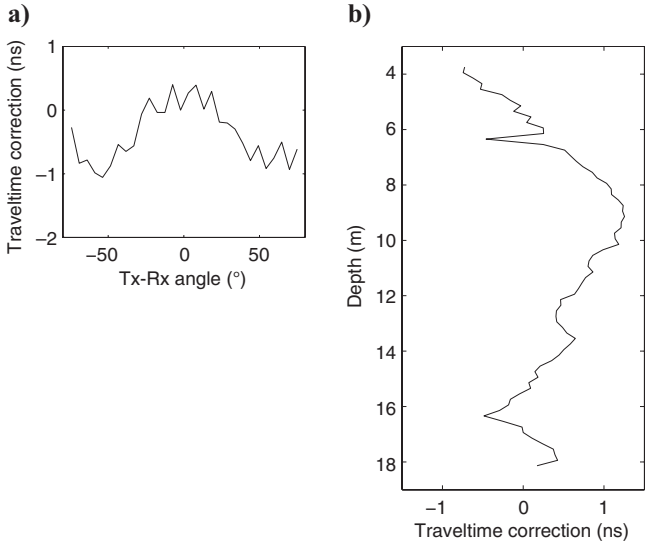

Figure 11. (a) Angle- and (b) receiver-position-dependent traveltime corrections obtained in the inversion of the BHRS data in Figure 10d.

As further verification of the validity of our tomographic inversion results, Figure 12 compares porosities obtained from the edges of the tomograms in Figure 10c and d with neutron-porosity logs collected in wells A1 and B2 at the BHRS. To convert the tomographic radar velocities to porosity values for the figure, we first converted them to bulk dielectric-constant values using the following low-loss equation:

$$\kappa_b = \frac{c^2}{v^2}, \tag{4}$$

where c is the velocity of light in free space. We then used the complex refractive index (CRIM) model (e.g., Huisman et al., 2003), given by

$$\kappa_b = [(1 - \theta)\kappa_s^\alpha + \theta\kappa_w^\alpha]^{1/\alpha} \tag{5}$$

to relate the dielectric constant to porosity, θ. Here, $\kappa_s = 4$ and $\kappa_w = 80$ were used for the dielectric constants of the mineral grains and water, respectively, and we set $\alpha = 0.5$. Solving equation 5 for θ, we have:

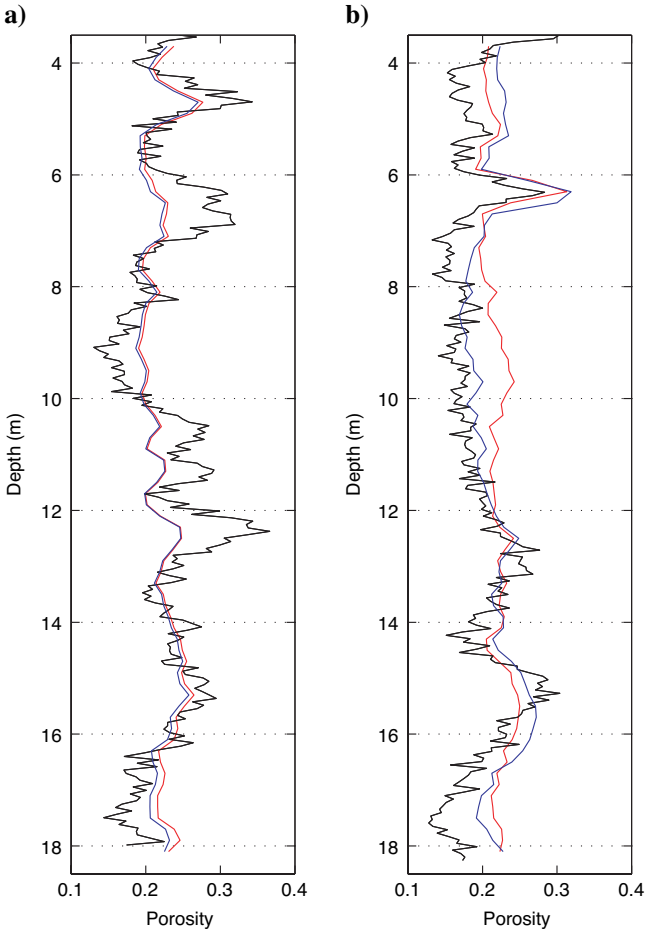

Figure 12. Comparison of neutron porosity log measurements (black), porosities calculated from velocites along the edges of the tomogram in Figure 10c (red), and porosities calculated from velocites along the edges of the tomogram in Figure 10d (blue). (a) Well A1 (transmitter); (b) Well B2 (receiver).

$$\theta = \frac{\kappa_b^\alpha - \kappa_s^\alpha}{\kappa_w^\alpha - \kappa_s^\alpha}. \tag{6}$$

Figure 12 shows that, except for a marked difference in amplitude because of the inherent smoothing in the ray-based tomographic velocity estimates, the tomographically derived porosities are quite well correlated with the porosity logs from each borehole. For well B2, we see that the tomographic results obtained using both angle- and receiver-position-dependent traveltime corrections are a significantly better match to the porosity data than the results with angle-dependent corrections alone. This further justifies our use of both types of traveltime corrections in creating Figure 10d.

CONCLUSIONS

Using an example data set from the BHRS, we have developed two strategies for improving the resolution of crosshole GPR tomography at close borehole spacings. Together, these strategies allow us to take full advantage of the excellent angular coverage that such borehole spacings can provide. For picking first breaks on very noisy traces at high transmitter/receiver angles, we have shown that a crosscorrelation approach using angle-dependent reference waveforms can be very effective. An important application of this picking method, not considered here, may be time-lapse crosshole GPR surveying, where the S/N is commonly very low because stacking of each trace is minimized for the sake of increased survey speed. As mentioned previously, our picking method performs best when strong scattering in the data (interfering with the direct arrivals) is not present. Future work includes investigating whether such an approach could be modified for effective use on other data sets containing strongly scattered events.

To incorporate high-angle data into crosshole GPR tomographic inversions, we have shown that inverting for a small number of parameters that describe an angle-dependent traveltime correction curve, in addition to subsurface velocities, can be very effective. We note again that this modified inversion procedure provided improved results with both synthetic and field data, despite the fact that only traveltimes were altered, and changes in survey geometry because of tip-to-tip antenna coupling were thus ignored. If necessary, the tomographic sensitivity matrix in equations 1–3 could also be adjusted to better account for end-to-end coupling above a certain threshold angle. This may be required with lower-frequency (i.e., longer antennas) data. An additional benefit of our inversion approach is that it allows us to correct for the effects of errors in transmitter fire time and borehole-location measurements. Although we believe that these measurements were very accurate for the BHRS data set, errors in these parameters also can result in apparent trends in velocity with angle at close borehole spacings, and thus incompatibility problems between high- and low-angle ray data.

Finally, we must stress that angular coverage is one of a number of factors that affect resolution in crosshole GPR tomography. By allowing for improved angular coverage with the methods presented here, we have seen that significant increases in tomographic resolution are possible. However, resolution with ray-based tomography can only be improved to a certain point, as ray-based techniques have an upper resolution limit of approximately the first Fresnel zone associated with the GPR pulse bandwidth. In order to improve resolution past this limit, finite-frequency (Fresnel-zone) or full-waveform inversion methods must be employed. Regardless, the use of high-angle data and angle-dependent traveltime corrections (as

described in this study) are critical to maximize the resolution of radar tomograms for hydrologic and environmental applications.

ACKNOWLEDGMENTS

This research was supported in part by funding to R. Knight from the National Science Foundation, Grant number EAR-0229896-002. J. Irving was also supported during part of this work through a Departmental Chair's Fellowship at Stanford University. The crosswell radar survey at the BHRS was funded by U. S. Army Research Office Grant DAAG5-98-1-0277 to M. Knoll. The authors would like to thank Peter Annan for many helpful discussions about antennas at the start of this research, and Warren Barrash for providing the neutron-porosity logs used in this study. The authors would also like to thank reviewers Sherif Hanafy, John Lane, and George Tsoflias for feedback that improved the manuscript.

REFERENCES

Alumbaugh, D., and P. Y. Chang, 2002, Estimating moisture contents in the vadose zone using cross-borehole ground-penetrating radar: A study of accuracy and repeatability: Water Resources Research, **38**, 1309; http://dx.doi.org/10.1029/2001WR000754.

Barrash, W., and T. Clemo, 2002, Hierarchical geostatistics and multi-facies systems: Boise Hydrogeophysical Research Site, Boise, Idaho: Water Resources Research, **38**, 1196; http://dx.doi.org/10.1029/2002WR001436.

Barrash, W., T. Clemo, and M. D. Knoll, 1999, Boise Hydrogeophysical Research Site: Objectives, design, and initial geostatistical results: Proceedings, Symposium on the Application of Geophysics to Engineering and Environmental Problems, 389–398.

Barrash, W., and M. D. Knoll, 1998, Design of research wellfield for calibrating geophysical methods against hydrologic parameters: Proceedings, Conference on Hazardous Waste Research, Great Plains/Rocky Mountains HSRC, 296–318; http://cgiss.boisestate.edu/%7Ebille/BHRS/Papers/Barrash98/Design98. html, accessed May 21, 2007.

Barrash, W., and E. C. Reboulet, 2004, Significance of porosity for stratigraphy and textural composition in subsurface coarse fluvial deposits, Boise Hydrogeophysical Research Site: Geological Society of America Bulletin, **116**, 1059–1073; http://dx.doi.org/10.1130/B25370.1.

Clement, W. P., and W. Barrash, 2006, Crosshole radar tomography in a fluvial aquifer near Boise, Idaho: Journal of Engineering and Environmental Geophysics, **11**, 171–184.

Clement, W. P., W. Barrash, and M. D. Knoll, 2006, Reflectivity modeling of ground-penetrating radar: Geophysics, **71**, no. 3, K59–K66.

Ellefsen, K. J., and D. L. Wright, 2005, Radiation pattern of a borehole radar antenna: Geophysics, **70**, no. 1, K1–K11.

Holliger, K., and T. Bergmann, 2002, Numerical modeling of borehole georadar data: Geophysics, **67**, 1249–1257.

Huisman, J. A., S. S. Hubbard, J. D. Redman, and A. P. Annan, 2003, Measuring soil water content with ground-penetrating radar: A review: Vadose Zone Journal **2**, 476–491.

Irving, J. D., and R. J. Knight, 2005a, Effect of antennas on velocity estimates obtained from crosshole GPR data: Geophysics, **70**, no. 5, K39–K42.

———, 2005b, Accounting for the effect of antenna length to improve crosshole GPR velocity estimates: 75th Annual International Meeting, SEG, Expanded Abstracts, 1188–1192.

———, 2006, Numerical simulation of antenna transmission and reception for crosshole ground-penetrating radar: Geophysics, **71**, no. 2, K37–K45.

Linde, N., A. Binley, A. Tryggvason, L. B. Pedersen, and A. Revil, 2006, Improved hydrogeophysical characterization using joint inversion of crosshole electrical resistance and ground-penetrating radar traveltime data: Water Resources Research, **42**, W12404; http://dx.doi.org/10.1029/2006WR005131.

Liu, S., and M. Sato, 2005, Transient radiation from an unloaded, finite dipole antenna in a borehole: Experimental and numerical results: Geophysics, **70**, no. 6, K43–K51.

Menke, W., 1984, The resolving power of cross-borehole tomography: Geophysical Research Letters, **11**, 105–108.

Molyneux, J. B., and D. R. Schmitt, 1999, First-break timing: Arrival onset times by direct correlation: Geophysics, **64**, 1492–1501.

Moret, G. J. M., M. D. Knoll, W. Barrash, and W. P. Clement, 2006, Investigating the stratigraphy of an alluvial aquifer using crosswell seismic traveltime tomography: Geophysics, **71**, no. 3, B63–B73.

Peraldi, R., and A. Clement, 1972, Digital processing of refraction data: Study of first arrivals: Geophysical Prospecting, **20**, 529–548.

Peterson, J. E., 2001, Pre-inversion corrections and analysis of radar tomographic data: Journal of Environmental and Engineering Geophysics, **6**, 1–18.

Pratt, R. G., and N. R. Goulty, 1991, Combining wave-equation imaging with travel-time tomography to form high-resolution images from crosshole data: Geophysics, **56**, 208–224.

Pratt, R. G., and M. H. Worthington, 1988, The application of diffraction tomography to cross-hole seismic data: Geophysics, **53**, 1284–1294.

Rector, J. W., and J. K. Washbourne, 1994, Characterization of resolution and uniqueness in crosswell direct-arrival traveltime tomography using the Fourier projection-slice theorem: Geophysics, **59**, 1642–1649.

Sato, M., and R. Thierbach, 1991, Analysis of a borehole radar in cross-hole mode: IEEE Transactions on Geoscience and Remote Sensing, **29**, 899–904.

Scales, J. A., 1987, Tomographic inversion via the conjugate gradient method: Geophysics, **52**, 179–185.

Squires, L. J., S. N. Blakeslee, and P. L. Stoff, 1992, The effects of statics on tomographic velocity reconstructions: Geophysics, **57**, 353–362.

Tronicke, J., P. Dietrich, and E. Appel, 2002a, Quality improvement of crosshole georadar tomography: Pre- and post-inversion data analysis strategies: European Journal of Environmental and Engineering Geophysics, **7**, 59–73.

Tronicke, J., P. Dietrich, U. Wahlig, and E. Appel, 2002b, Integrating surface georadar and crosshole radar tomography: A validation experiment in braided stream deposits: Geophysics, **67**, 1516–1523.

Tronicke, J., K. Holliger, W. Barrash, and M. D. Knoll, 2004, Multivariate analysis of cross-hole georadar velocity and attenuation tomograms for aquifer zonation: Water Resources Research, **40**, W01519; http://dx.doi.org/10.1029/2003WR002031.

VanDecar, J., and R. Crosson, 1990, Determination of teleseismic relative phase arrival times using multi-channel cross-correlation and least squares: Bulletin of the Seimological Society of America, **80**, 150–159.

Vasco, D. W., J. E. Peterson, and K. H. Lee, 1997, Ground-penetrating radar velocity tomography in heterogeneous anisotropic media: Geophysics, **62**, 1758–1773.

Woodward, R. L., and G. Masters, 1991, Global upper mantle structure from long-period differential arrival times: Journal of Geophysical Research, **96**, 6351–6377.